

Phosphine-Protected Atomically Precise Silver–Gold Alloy Nanoclusters and Their Luminescent Superstructures

Madhuri Jash, Arijit Jana, Ajay K. Poonia, Esma Khatun, Papri Chakraborty, Ankit Nagar, Tripti Ahuja, K. V. Adarsh,* and Thalappil Pradeep*



Cite This: <https://doi.org/10.1021/acs.chemmater.2c03222>



Read Online

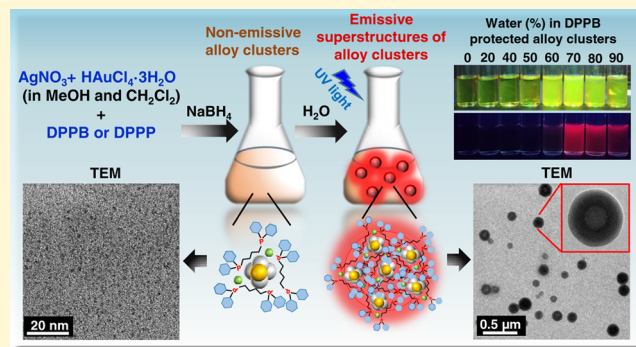
ACCESS |

Metrics & More

Article Recommendations

Supporting Information

ABSTRACT: Superstructures made by assemblies of metal nanoclusters (NCs) have gained interest due to their atomic precision and exciting photophysical properties. Although there are some reports of cluster-assembled materials of NCs protected with thiols, the preparation of stable thiol-free analogs is largely unexplored due to the poor stability of such structures. Herein, we report the synthesis of phosphine-protected alloy NCs of silver with varying gold doping and superstructures of such systems. We show that alloying of phosphine-protected silver clusters with gold results in comparatively more stable clusters than weakly ligated hydride- and phosphine-coprotected silver clusters. Two new Ag–Au alloy cluster series, $[\text{Ag}_{11-x}\text{Au}_x(\text{DPPB})_5\text{Cl}_5\text{O}_2]^{2+}$, where $x = 1-10$ ($\text{Ag}_{11-x}\text{Au}_x$ in short), and $[\text{Ag}_{15-x}\text{Au}_x(\text{DPPP})_6\text{Cl}_5]^{2+}$, where $x = 1-6$ ($\text{Ag}_{15-x}\text{Au}_x$ in short), have been synthesized using two different phosphines, 1,4-bis(diphenylphosphino)butane (DPPB) and 1,3-bis(diphenylphosphino)propane (DPPP), respectively. These alloy clusters possess aggregation-induced emission (AIE) property, which was unexplored till now for phosphine-protected silver clusters. A visibly nonluminescent methanol solution of these clusters showed strong red luminescence in the presence of water due to the formation of cluster-assembled spherical hollow superstructures without any template. A solvophobic effect along with $\pi\cdots\pi$ and C–H $\cdots\pi$ interactions in the ligand shell make the alloy NCs assemble compactly within the hollow spheres. The assembly makes them highly emitting due to the restriction of intramolecular motion. The emissive states of the alloy clusters show a many-fold increase in lifetime in the presence of water. Femtosecond transient absorption studies revealed the lifetime of the excited-state charge carriers in their monomeric and aggregated states. Apart from enriching the limited family of phosphine-protected silver alloy NCs, this work also provides a new strategy to build a controlled assembly of NCs with tailored luminescence. These materials could be new phosphors for applications in composites, sensors, thin films, and photonic materials.



INTRODUCTION

Metal nanoclusters (NCs) are molecular entities composed of a few to tens of metal atoms in their core. As their sizes decrease to the Fermi wavelength of electrons in the specific metal, discrete electronic states appear in them.^{1–3} As a result, these ultrasmall NCs become sensitive to particle size, even to the extent of a single atom.⁴ Metal NCs with atomic precision have been synthesized successfully by various research groups in the last two decades. They exhibit several unique properties, such as quantized charging,⁵ magnetism,⁶ luminescence,⁷ chirality,⁸ and so on, compared to their bulk counterparts. Among them, luminescence is the most remarkable property of such NCs due to applications in chemical sensing,⁹ optoelectronics,¹⁰ biosensing and bioimaging,¹¹ etc. Thus, the synthesis of highly luminescent NCs with good photostability, large Stokes shift, tunable emissive property, low toxicity, and biocompatibility is extremely important. However, poor stability and weak luminescence of NCs are limiting

factors for their practical applications. To overcome these issues, several synthetic strategies have been followed, and alloying of metal clusters is one of them.^{12,13} Compositional tuning of NCs by doping with other metals offers a way to improve their luminescence property along with stability, and therefore, the topic has attracted intense research interest.^{14–16}

The photophysical properties of luminescent NCs have been investigated mainly in solution, and there are several reports on this.^{17–19} Their solid-state luminescence has also gained significant interest in the fields of light-emitting diodes (LEDs)^{20–22} and sensors.^{23–25} Aggregation-induced emission

Received: October 25, 2022

Revised: December 14, 2022

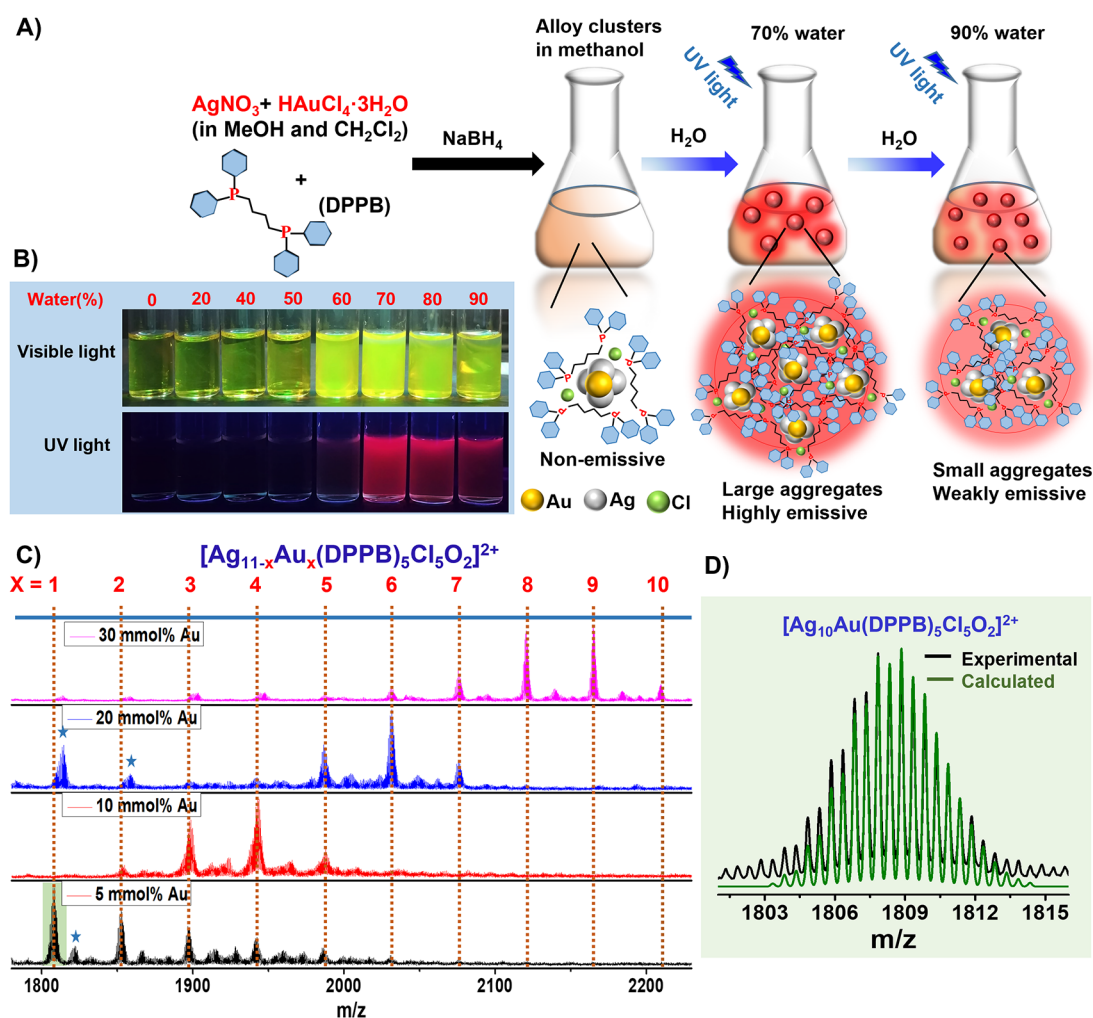


Figure 1. (A) Schematic illustration of the synthesis of the $Ag_{11-x}Au_x$ clusters and the formation of luminescent spheres due to solvent-induced aggregation. (B) Corresponding photographs of the samples with different water fractions under visible light and UV light. (C) Positive-mode electrospray ionization mass spectrometry (ESI MS) of $[Ag_{11-x}Au_x(DPPB)_5Cl_5O_2]^{2+}$ ($x = 1-10$), synthesized by varying the doped Au from 5 to 30 mmol %. The peaks labeled * refer to fragmented species. (D) Comparison of the experimental and calculated isotopic distributions of the cluster $[Ag_{11-x}Au_x(DPPB)_5Cl_5O_2]^{2+}$, when $x = 1$.

(AIE) has been a promising strategy for luminescence enhancement in the solid and solution states to fabricate novel photoluminescent materials.^{26–31} AIE was discovered by Tang's group in 2001, and it mainly occurs due to the restriction of intramolecular motion, thus reducing the nonradiative relaxation pathways.³² For metal NCs, in their aggregated state, due to the metallophilic interaction and/or suppressed molecular motion of ligands, radiative relaxation pathways are greatly enhanced, which result in luminescence enhancement with high quantum yield, large Stokes shift, higher emissive lifetime, and high chemical stability. Because of the AIE phenomenon, the construction of hierarchical self-assembly of NCs has been explored to achieve higher brightness compared to their elementary components. This self-assembly is an effective strategy to regulate the spatial distribution of NCs to form regular superstructures so that their luminescence property can be tuned. This approach involves the right balance of intercluster interactions, which are mainly attractive forces between the surface ligands or motifs of different NCs.^{33–36}

As the properties^{2,3} and reactivities³⁷ of metal NCs can be changed dramatically by changing the capping ligands, the nature of surface ligands also plays an important role in manipulating the attractive forces (metallophilic, electrostatic, dipole–dipole, hydrogen bonding, and hydrophobic interactions) to drive the formation of NC-assembled superstructures.^{33–36} However, it has also been demonstrated that metal doping can reconstruct the metal–ligand motif and thus facilitate the radiative relaxation pathway of the excited electrons.^{38,39} Furthermore, the emission energy of the cluster-assembled structures depends on the interatomic distance as well as the compactness of the superstructures.⁴⁰ The process of self-assembly can also be induced by external stimuli like metal ions, solvents, light, temperature, polymers, pH, etc.³⁴ These cluster-assembled superstructures provide innovative approaches in the field of LEDs, sensing, bioimaging, and theranostics.³⁴ They also have advantages over discrete NCs in terms of their sensitivity, photostability, and cellular retention. Therefore, creating self-assembly of different classes of metal NCs is necessary to better understand their structural details, associated luminescence enhancement,

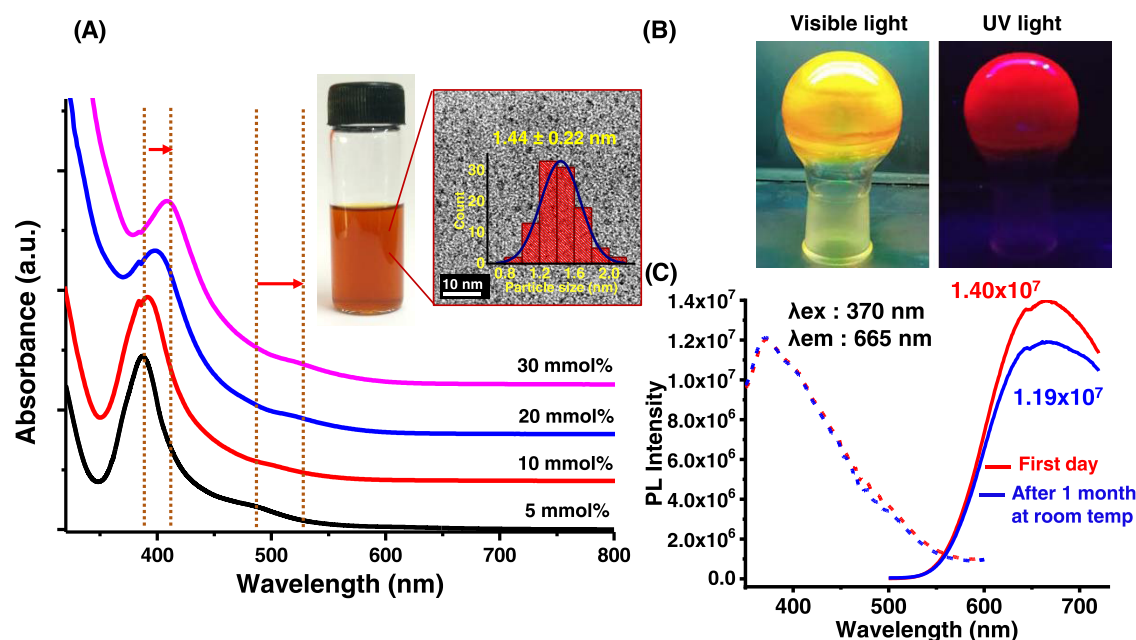


Figure 2. (A) UV-vis absorption spectra of the $\text{Ag}_{11-x}\text{Au}_x$ clusters by varying the amount of doped gold from 5 to 30 mmol %. The shift in peak position is marked. The change in absorbance at 386 nm is due to a lamp change. Inset: photograph of cluster 1 in methanol (under visible light) with TEM micrograph and particle size distribution. (B) Photographs of the solid-state cluster 1 (vacuum dried) under visible light and UV light. (C) Excitation (dotted line) and emission spectra (solid line) of 1 in the solid state show room-temperature stability of the cluster.

and potential applications. However, there is limited diversity of ligands in making these self-assembled luminescent superstructures of metal clusters, and as of now, the most preferred choice for such structures is thiolate-protected NCs. Therefore, besides the fundamental interest in using different kinds of ligands in cluster-assembled materials, there is also interest in controlling the size, structure, density, and AIE properties of their assembled structures.

Herein, we have synthesized two new series of Ag-Au alloy NCs to explore the diversity and photophysical properties of phosphine-protected clusters in the absence of any thiolate ligand. During the synthesis, the concentration of incoming Au precursor was varied with two different phosphines, and the compositions of these two alloy cluster series were assigned as $[\text{Ag}_{11-x}\text{Au}_x(\text{DPPB})_5\text{Cl}_5\text{O}_2]^{2+}$, where $x = 1-10$, and $[\text{Ag}_{15-x}\text{Au}_x(\text{DPPP})_6\text{Cl}_5]^{2+}$, where $x = 1-6$, from their high-resolution electrospray ionization mass spectrometry (HRESI MS) data. These clusters are referred to as $\text{Ag}_{11-x}\text{Au}_x$ and $\text{Ag}_{15-x}\text{Au}_x$ respectively, in discussion. The most important finding here is the emergence of the AIE property of these phosphine-protected alloy clusters. We note that there are two reports of the AIE of phosphine-protected gold clusters but without any confined superstructures.^{41,42} In this study, the silver-rich alloy clusters form luminescent hollow superstructures in their aggregated state, confirmed by dynamic light scattering (DLS), transmission electron microscopy (TEM), field emission scanning electron microscopy (FESEM), and hyperspectral imaging (HSI). Aggregates exhibit characteristic signatures in photoluminescence (PL) spectroscopy. The PL lifetimes of these cluster aggregates have also been determined using time-correlated single-photon counting (TCSPC) measurements. To further understand the excited-state relaxation dynamics of these alloy clusters, we have performed femtosecond transient absorption (fs-TA) spectroscopy for different forms (monomeric and aggregated) of the clusters. Thus, this work offers a strategy to build

spherical luminescent superstructures from atomically precise phosphine-protected alloy NCs along with an understanding of their structures and photophysical properties.

RESULTS AND DISCUSSION

Synthesis of Phosphine-Protected Alloy Clusters and their AIE Property. We have synthesized phosphine- and chlorine-coprotected Ag-Au alloy NCs using a single-step coreduction method. So far, there is only one report of phosphine- and chlorine-protected heteroatom (Pt)-doped silver cluster using a single-step reaction.⁴³ Here, both the alloy NC series, $\text{Ag}_{11-x}\text{Au}_x$ and $\text{Ag}_{15-x}\text{Au}_x$ were synthesized by coreducing the mixture of silver and gold precursors in the presence of diphosphine ligands in CH_3OH and CH_2Cl_2 as cosolvents. A detailed synthetic procedure is given in the [Experimental Section](#). During the synthesis of $\text{Ag}_{11-x}\text{Au}_x$ after 8 h of reaction in the dark, the monomeric mixed alloy clusters were formed, and they were nonluminescent under UV light. An important finding of these phosphine-protected alloy NCs was that they generated strong luminescence in the solid state and in the presence of a poor solvent, namely, water, due to aggregation. In the absence of the gold precursor, the same reaction resulted in a hydride- and phosphine-protected $[\text{Ag}_{27}\text{H}_{22}(\text{DPPB})_7]^{3+}$ cluster, which was nonluminescent both in the solution and in the aggregated state (in the aqueous phase). This comparatively less stable hydride and 1,4-bis(diphenylphosphino)butane (DPPB)-coprotected silver cluster was already reported by our group.⁴⁴ In this work, the luminescence intensity of the aggregated Ag-Au alloy clusters can be altered by changing the fraction of water ($f_w = \text{vol } \% \text{ of water}$) in the methanol/water mixture due to the formation of differently sized aggregates. A schematic of the same is presented in [Figure 1A](#) for the $\text{Ag}_{11-x}\text{Au}_x$ clusters. The corresponding photographs of the samples under visible and UV light are shown in [Figure 1B](#).

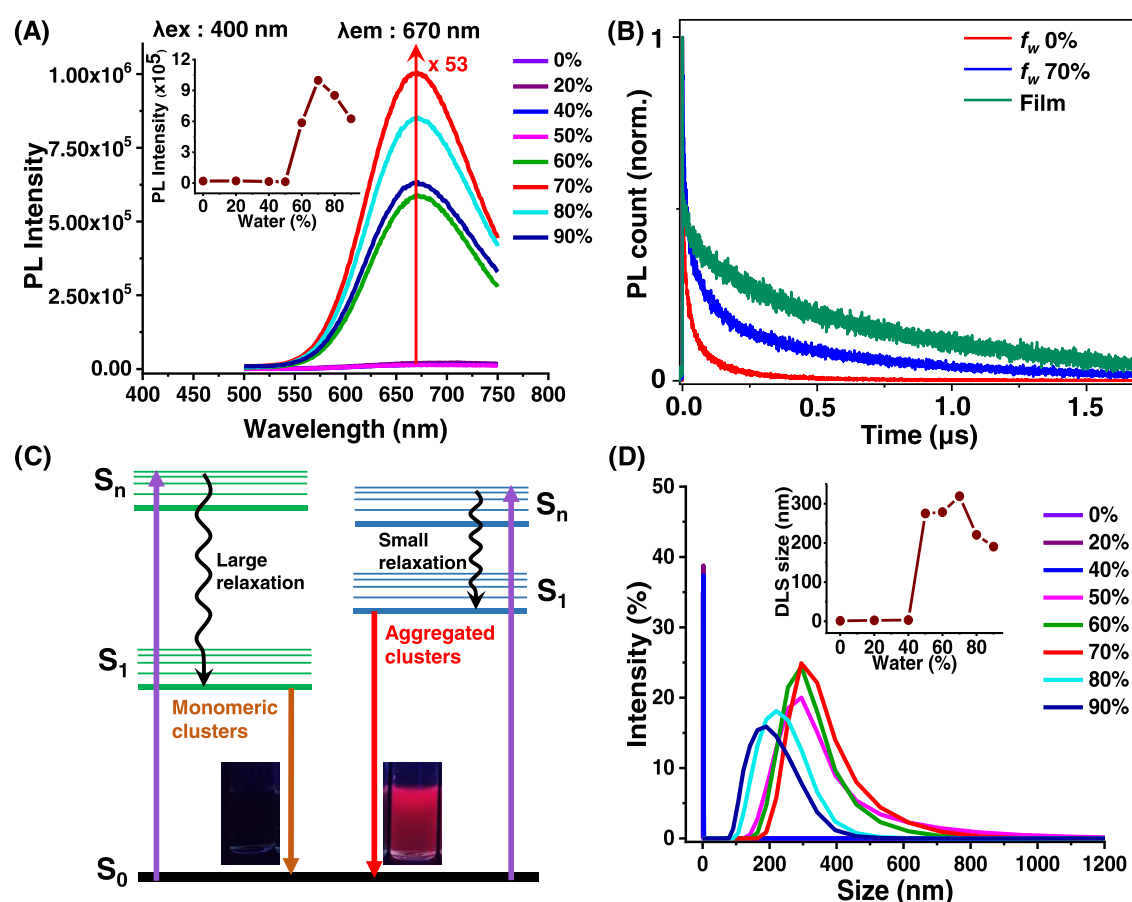


Figure 3. (A) PL emission spectra of **1** in methanol/water mixtures with different fractions of water. Inset: variation of luminescence intensity of the aggregates at different water fractions. (B) PL decay curves measured by TCSPC for f_w 0%, 70%, and film of cluster **1**. (C) Schematic diagram showing the PL decay pathways of cluster **1** at different states. (D) DLS data of **1** in methanol/water mixtures with different fractions of water. Inset: variation of DLS size of the aggregates at different water fractions.

Characterization of the $\text{Ag}_{11-x}\text{Au}_x$ Clusters. For characterization of the $\text{Ag}_{11-x}\text{Au}_x$ clusters, the concentration of incoming Au precursor was varied from 5 to 30 mmol % to know the maximum doping position of Au in the alloy cluster core. Figure 1C represents the positive-mode HRESI MS data, where 5 mmol % Au doping exhibited a group of peaks in +2 charge state. Each of the peaks of this group was separated by m/z 44.5, with a total mass difference of $\Delta m = 44.5 \times 2 = 89$ ($z = 2$). This mass difference signified a sequential replacement of Ag atoms in the parent cluster with Au atoms. Here, among the five peaks, the first sharp peak appeared at m/z 1808.0, and the last peak appeared at a mass difference of $\Delta m = 357$ ($\Delta m/z = 178.5$, $z = 2$), which indicates that 4 Ag atoms were replaced with Au atoms. The cluster composition was assigned as $[\text{Ag}_{11-x}\text{Au}_x(\text{DPPB})_5\text{Cl}_5\text{O}_2]^{2+}$, where $x = 1-5$ for 5 mmol % Au. The origin of oxygen can be from the solvent or from the atmosphere. The mass spectrometric composition of the alloy clusters was further confirmed by the exact matching of the experimental spectrum with the calculated isotopic patterns of each of the species. Figure 1D represents the comparison between the experimental and calculated spectra of $[\text{Ag}_{11-x}\text{Au}_x(\text{DPPB})_5\text{Cl}_5\text{O}_2]^{2+}$ when $x = 1$. By increasing the amount of doped Au from 5 to 30 mmol %, we were able to incorporate a maximum of 10 Au atoms in the alloy clusters, and the total composition was assigned as $[\text{Ag}_{11-x}\text{Au}_x(\text{DPPB})_5\text{Cl}_5\text{O}_2]^{2+}$, where $x = 1-10$.

Optical characterization of the $\text{Ag}_{11-x}\text{Au}_x$ clusters was carried out by UV-vis and PL spectroscopy. The UV-vis spectra of 5–30 mmol % of Au doping are shown in Figure 2A. With increasing Au incorporation in the alloy cluster, the main absorption peak was red-shifted from 387 to 409 nm, and the shoulder peak was red-shifted from 485 to 520 nm, which is attributed to a reduction in the highest occupied molecular orbital–lowest unoccupied molecular orbital (HOMO–LUMO) gap.^{45,46} During this Au incorporation, both the absorption peaks were broadened, while the shape of all of the spectra remained the same, indicating successful Au doping in the Ag NCs and similar geometrical structures for all of the alloy clusters. These nonluminescent alloy NCs were orange in color in methanol, and for 5 mmol % Au doping, the average size of the particles was found to be 1.4 ± 0.2 nm in the TEM images (inset of Figure 2A). All of the $\text{Ag}_{11-x}\text{Au}_x$ clusters with 5–30 mmol % Au doping showed AIE; for ease of measurement, alloy clusters with 5 mmol % gold doping were selected for further characterization and labeled as **1**. The methanol solution of **1** was nonemissive to the naked eye and very weakly emissive in the PL spectrum with a large Stokes shift, as shown in Figure S1. Interestingly, when the methanol solution was vacuum dried to get the cluster in the solid state, it showed strong red luminescence under UV light, as shown in Figure 2B. Excitation and emission spectra of **1** in the solid state have been recorded by drop-casting a methanol solution on a glass slide and making a film. The excitation wavelength

was 370 nm, and the emission wavelength was 665 nm, as shown in Figure 2C. This large Stokes shift (>250 nm) can minimize reabsorption losses during their application as solid-state emitters. To further investigate the stability of this solid-state alloy NCs, PL spectra of the same sample (film on a glass slide) were recorded after storing it in the dark and at room temperature for 1 month. After 1 month also, it emitted strong red luminescence at 665 nm, where the PL intensity was decreased from 1.40×10^7 to 1.19×10^7 (15%). UV-vis spectra of this sample were also recorded before and after 1 month, as shown in Figure S2.

For characterization of **1**, ^{31}P nuclear magnetic resonance (NMR) spectroscopy was performed, and the data were compared with that of the ligand DPPB (Figure S3). The appearance of two new broad peaks at -1.21 and -3.27 ppm confirmed the formation of a bond between phosphine and the alloy metal core. More than one new peak also indicated the different ligand environments in **1**, and the disappearance of the peak at -16.15 ppm confirmed the absence of any free phosphine ligand in the NCs. X-ray photoelectron spectroscopy (XPS) measurements were carried out to know the chemical state of Au and Ag in the alloy NCs. In Figure S4A, the XPS survey spectrum confirms the presence of elements C, O, P, Cl, Ag, and Au. The specific regions of Ag, Au, P, and Cl are deconvoluted in Figure S4B–E, respectively. The Ag $3d_{5/2}$ peak appeared at 367.8 eV (i.e., oxidation side), which is slightly lower than the metallic Ag(0) value (368.0 eV), suggesting that the metal is between Ag(0) and Ag(I). The Au $4f_{7/2}$ peak appeared at 85.4 eV, which is higher than the metallic Au(0) value (84.0 eV) and suggested that doped Au was present as Au(I).⁴⁷ The position of the Au $4f_{7/2}$ peak indicates that the doping position of Au in the alloy cluster is not at the center; instead, it is at the outer shell of the cluster core, attached to the ligands. Transmission electron microscopy energy-dispersive X-ray spectroscopy (TEM EDS) analysis also confirmed the presence of Ag, Au, P, and Cl in **1** (Figure S5).

Solvent-Induced Aggregation of the $\text{Ag}_{11-x}\text{Au}_x$ Clusters. For the solvent-induced aggregation, we have already observed that by adding different vol % of water to the methanol solution of the cluster, different luminescence intensities appear. To check their luminescence property, PL spectra were collected (for samples with different f_w) upon excitation at 400 nm with a cluster concentration of 1 mg/mL (Figure 3A). The emission peak was blue-shifted from 695 to 670 nm when f_w was varied from 0 to 90%. During the addition of water, strong emission of the sample did not appear until f_w reached 60%, and an emission maximum appeared at 670 nm. The PL intensity reached its maximum value when f_w was 70% with 53-fold luminescence enhancement. This enhancement might be due to the $\pi\cdots\pi$ and C–H $\cdots\pi$ interactions of the phosphine ligands induced by the solvophobic effect, which restrict the intramolecular motion of the bulky phosphine ligands in the aggregated state.^{48,49} Afterward, the luminescence intensity was gradually reduced from f_w 70 to 90%, and the emission peak position appeared constant at 670 nm.⁵⁰ The inset of Figure 3A shows the variation of PL intensity at 670 nm with changing fractions of water. The UV-vis spectra for these solutions showed a small red shift for both the main peak and the shoulder peak after the formation of aggregates. Though there was a visible decrease in molar absorptivity due to the formation of aggregates, no change was observed in the absorption peak pattern (Figure

S6).⁵¹ Notably, apart from the PL enhancement, aggregation of NCs also causes the manipulation of PL lifetime. To monitor it, we have measured the PL lifetime using TCSPC spectroscopy (instrumental details are given in the Supporting Information (SI)). The acquired PL decay curves of **1** in monomeric (in methanol or f_w 0%), water-aggregated (f_w 70%), and solid (film) states are shown in Figure 3B. It clearly shows the significant increase in the lifetime for aggregates in water and solid states of cluster **1** in comparison to the monomeric form. To determine the corresponding lifetime, TCSPC curves were fitted with the exponential function

$$y = y_0 + \sum_i^n A_i e^{-(t/\tau_i)}$$

and the average decay constants were calculated using

$$\tau_{\text{avg}} = \frac{\sum_i^n A_i \tau_i}{\sum_i^n A_i}$$

The average lifetime values of monomeric, water aggregates, and solid states were 26.8, 131.8, and 311.4 ns, respectively (see Table S1 for details).

To verify the nature of the excited state, the PL intensity of water aggregates of **1** was checked after oxygen exposure. The PL spectra were almost identical before and after oxygen-saturated conditions (Figure S7), which implies that this photophysical phenomenon is fluorescence in nature.⁵² Here, the monomeric cluster **1** in methanol (f_w 0%) exhibits emission maximum at 695 nm, whereas the water-aggregated (f_w 70%) and solid-state film show almost the same blue-shifted peak position at 670 and 665 nm, respectively. Therefore, cluster **1** in methanol relaxes from a low-lying singlet state to S_0 with 695 nm emission, and the nonradiative relaxation pathways become more dominant than the radiative pathways. At a higher water fraction (f_w 70%) and in the solid state, there was the suppression of free rotation and vibration of the ligands in the cluster aggregates, which reduced the nonradiative relaxation pathways, and radiative decay occurred from a high-lying singlet state to S_0 with an emission at 670 nm.⁵³ A schematic diagram of the PL decay pathway of cluster **1** at different states is shown in Figure 3C.

Characterization of the Aggregated Structures of $\text{Ag}_{11-x}\text{Au}_x$ Clusters. To examine the sizes of these aggregates in the solvent mixtures, DLS experiments were performed, and the data are shown in Figure 3D. The DLS data indicated that for up to f_w 40%, the particle sizes were in the range of 1–4 nm, which is in the size range of ligand-protected NCs in solution without any aggregation. For f_w 50%, the aggregates started to form, and an average hydrodynamic diameter of ca. 280 nm was seen. Upon further increasing f_w to 60 and 70%, the average hydrodynamic diameters of the aggregates increased to ca. 290 and 315 nm, respectively, along with an increase in the PL intensity. The aggregates gradually decreased in size from f_w 70 to 90% and gave a reduced diameter of ca. 180 nm, along with a reduced PL intensity. Hence, the difference in the luminescence intensity can be attributed to the different aggregation diameters of the clusters formed at different polarities of solvents.⁵⁰ The inset of Figure 3D shows the variation of DLS size of the particles with changing fractions of water.

To know more about the packing of clusters in these nanoscale aggregates, TEM images were collected for the solutions of different f_w values along with their average particle

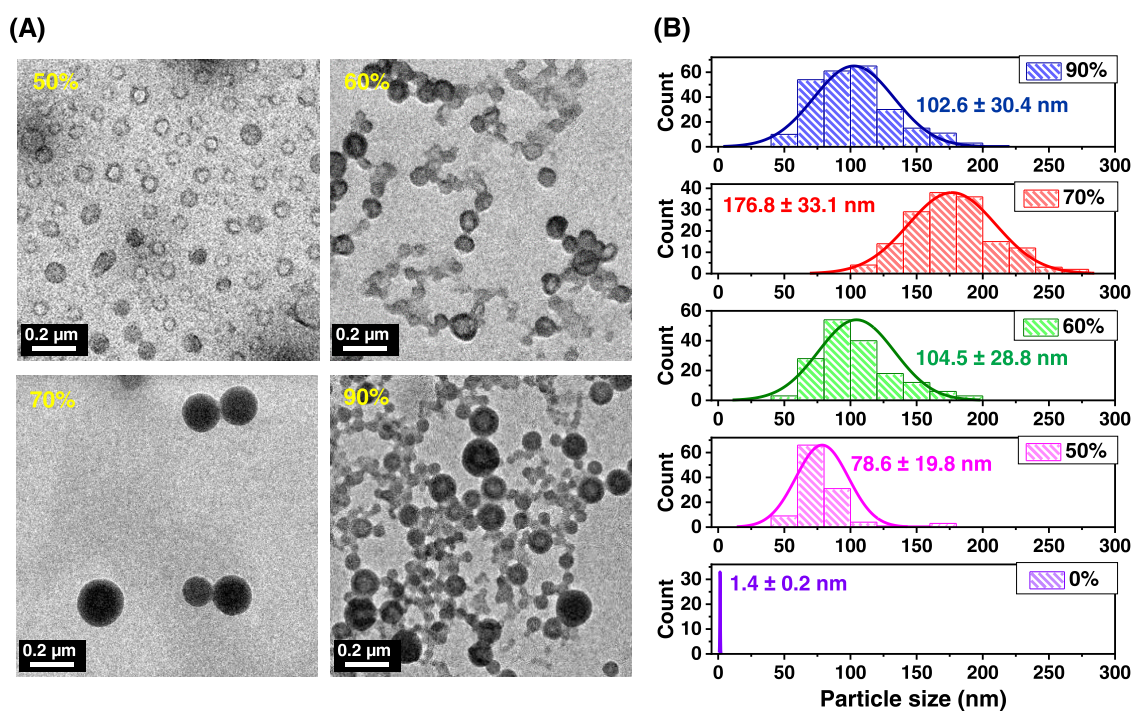


Figure 4. (A) TEM images of **1** during the formation of solvent-induced aggregates in the presence of 50, 60, 70, and 90% water. (B) Evolution of particle size distribution by increasing the water fraction in a methanol/water mixture.

sizes (Figure 4A,B). The spherical aggregates started to be observed when f_w reached 50%, and the clusters were loosely assembled in spheres of 78.6 ± 19.8 nm diameter. At f_w 60%, the average size of the aggregates increased to 104.5 ± 28.8 nm, and at f_w 70%, the average size became 176.8 ± 33.1 nm. As observed from TEM images, upon increasing f_w from 50 to 70%, the sizes of aggregates become larger, denser, and solely spherical. For f_w 90%, the average size of the spheres decreased to 102.6 ± 30.4 nm and became less dense compared to the structures formed at f_w 70%. Here, the larger and denser the aggregates, the higher the amount of restricted intra- and intermolecular motions and the brighter the luminescence would be. Thus, it was concluded that the ratio of methanol/water in the solution plays an important role in modulating the size of the aggregates, which leads to variation in their PL intensity.

At f_w 70%, the sample exhibited the highest luminescence intensity due to the formation of bigger and denser spherical aggregates, and these structures were closely monitored with a transmission electron microscope and a field emission scanning electron microscope. In Figure 5A, we can see the formation of discrete spheres under TEM, which has been discussed before. Figure 5B represents a higher magnified view of a single sphere, whereas the inset of Figure 5A clearly shows that these spheres are actually made up of the assembly of small NCs. These spheres are hollow in nature, forming vesicle-like structures. They have visible peripheral and interior domains, and the former can be made by the assembly of NCs with varying packing densities. The inner layer of the periphery was denser compared to the outer layer, which sealed the hollow interior space. More TEM images of hollow spheres with different magnifications are shown in Figure S8A. However, the thickness of the peripheral bilayer can vary from one sphere to another, and they can be connected with each other through the outer layer of their periphery (Figure S8B). Figure

5C represents the TEM EDS of the aggregates, which shows the presence of all elements Ag, Au, P, and Cl along with their wt % and atom %. The morphology and size of these aggregates were also analyzed by FESEM after sputter coating the samples with Au–Pd. Figure 5D represents a large area view, whereas Figure 5E presents a magnified view of a single sphere. As SEM focuses on the surface, it shows only the spherical shape of the aggregates and does not show the interior hollow morphology as in TEM. The distribution of elements on a single sphere was examined using line scan profiles of the FESEM (Figure 5F). All of the elements (Ag, Au, P, Cl) were detected in the line scan, and the atomic ratio matches well with the atomic ratio of the alloy cluster except Au, which arises due to Au–Pd sputtering. During a line scan through the center of the sphere, the signals for all of the elements enhanced significantly across the sphere, as expected. The stability of these superstructures was checked after 1 week, and they were stable in the solution and solid states, as shown in Figure S9. The spatial distribution of these spheres was investigated by dark-field microscopy (Figure 5G), along with fluorescence microscopy (Figure 5H). A broadband white light was used as the source for hyperspectral imaging, where the light scattered by a single sphere was light green in color. Figure 5I presents the measured average scattering spectrum centered at 502 nm. The fluorescence micrograph showed that each sphere is red luminescent.

Mechanism of the Formation of Superstructures. The mechanism of the formation of such hollow spherical superstructures can be attributed to the presence of hydrophilic (Cl) and hydrophobic (diphosphine) ligands in the ligand shell of the alloy clusters. According to the directionality of these two types of ligands, there can be breaking of the spherical symmetry of the ligands, and thus, clusters can have some amphiphilic character.^{54,55} The $\pi \cdots \pi$ and C–H \cdots π interactions among the diphosphine ligands of alloy clusters

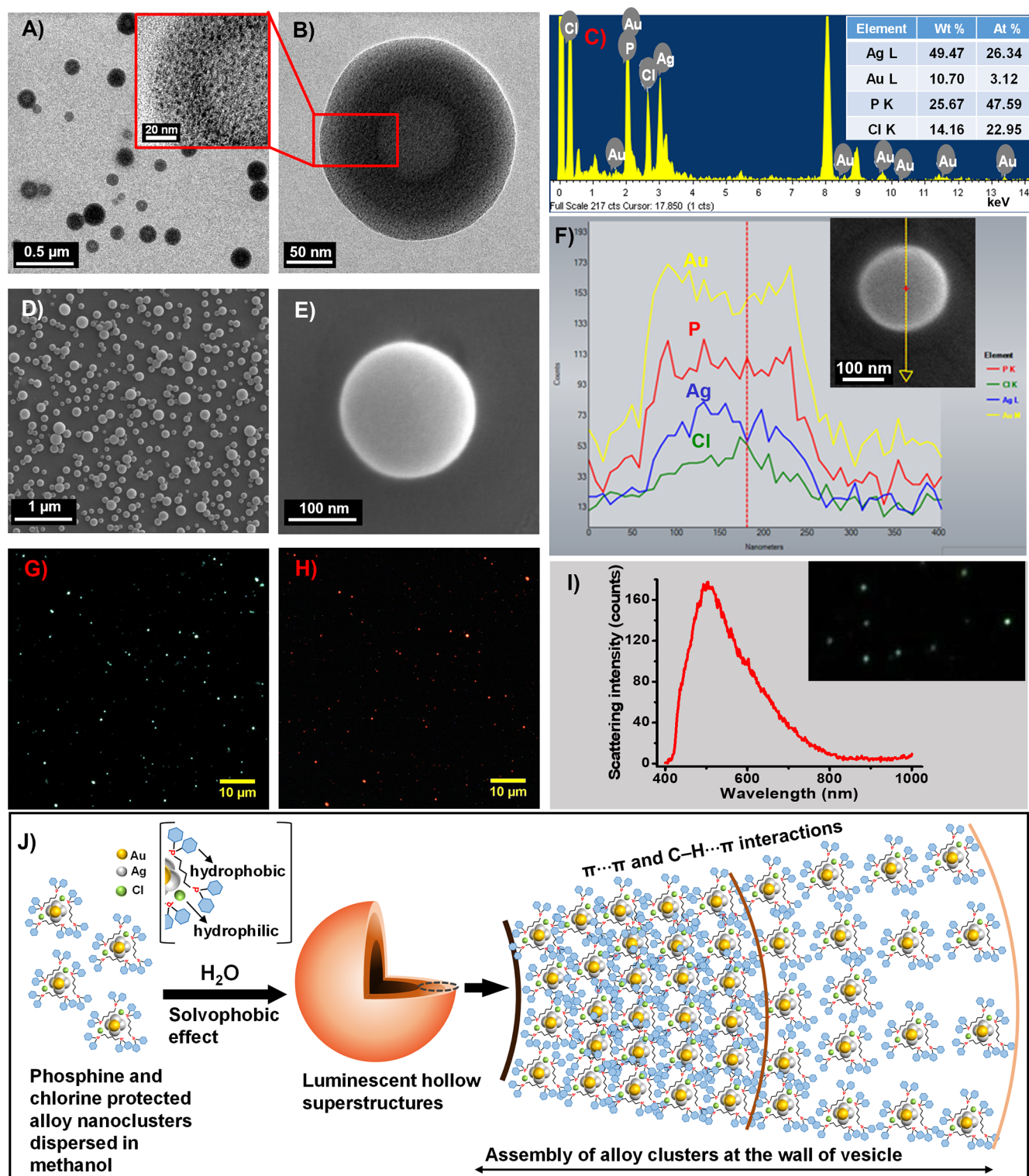


Figure 5. Microscopic characterization of the aggregates of **1** formed at f_w 70%. (A, B) TEM images of the spheres with different magnifications. (C) TEM EDS spectrum and elemental composition of the aggregates. (D, E) FESEM images with different magnifications. (F) SEM EDS line scan is measured along a single sphere indicated by the arrow. (G) Dark-field and (H) fluorescence micrograph of the cluster aggregates, immobilized on an ultraclean glass slide. (I) Average scattering spectrum of the aggregates. (J) Schematic illustration of the possible assembly of clusters within the superstructures.

may contribute to the stabilization and growth of the cluster assembly.⁵⁶ Therefore, to achieve minimum surface energy, the assembly of amphiphilic NCs might tend to attain a spherical shape and make hollow vesicle structures.^{57,58} Such an

assembly of clusters can be tuned by changing the solvent polarity. Based on the TEM result of superstructures, the NCs are located in the wall region of hollow vesicles. By increasing the water content, the wall becomes thicker, presumably to

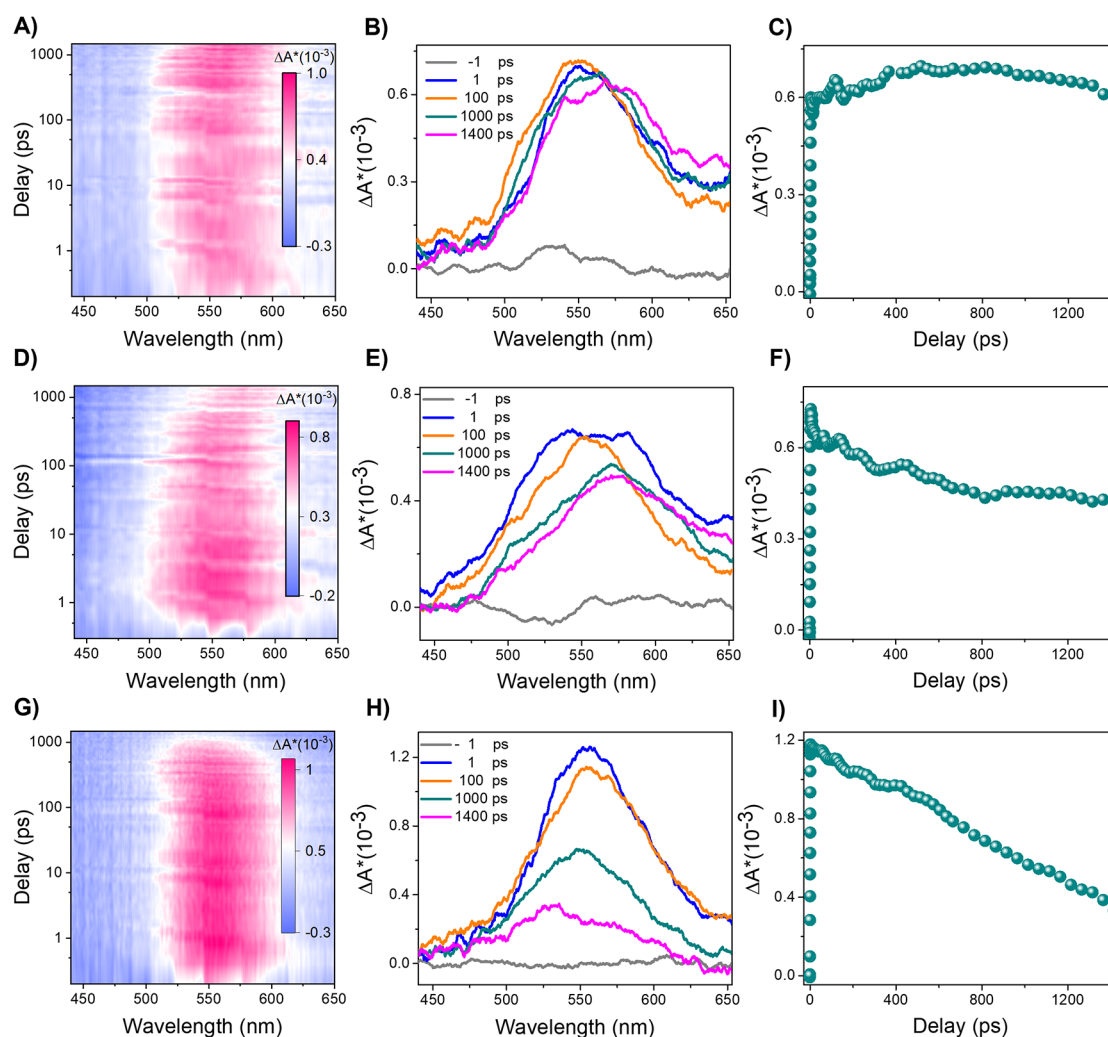


Figure 6. fs-TA pump–probe spectra of **1**. (A) Contour plot, (B) TA spectral profile as a function of time delay, and (C) transient kinetic trace at a selected wavelength of 552 nm for **1** in methanol. The same measurements have also been done for the aggregates formed at f_w 70% (D–F) and in the solid state (G–I).

reduce the contact between NCs and highly polar solvent water, which has been seen for f_w 50–70% in Figure 4A. For f_w 90%, due to very high solvent polarity, the aggregate formation of **1** can be very fast, which can decrease the effective size of the spheres.⁵¹ A schematic illustration of the possible assembly of clusters within the superstructures is presented in Figure S1J.

TA Spectroscopy of the Monomeric and Aggregated Forms of $\text{Ag}_{11-x}\text{Au}_x$ Clusters. We have performed fs-TA spectroscopy to further understand the excited-state electronic transition of **1** in methanol and in aggregated states (with water and thin film). Our setup consists of pumping the carriers from HOMO to LUMO using an intense pump beam and then investigating the carrier's excited state and relaxation dynamics using a probe pulse. In the experiments, samples were first excited using a 120 fs pulse with a pump fluence of $127 \mu\text{J}/\text{cm}^2$ centered at 400 nm. Then, a broadband pulse (440–655 nm), delayed with respect to the pump pulse, was used to probe the time evolution of carriers in the excited states. The instrumental setup and measurement details are given in the SI. Figure 6A–C summarizes the TA data of **1** in methanol. The contour plot of TA is in Figure 6A, and spectral profiles at selected time delays are plotted in Figure 6B, where the observed prominent feature is a band of photoinduced

absorption (PIA). Interestingly, no ground-state photobleaching (GSPB) (due to the Pauli blocking of electronic state by pump excited carriers) was observed corresponding to the UV–vis peak in the regime of 500 nm, which manifests the dominance of excited-state transitions in **1**, similar to the behavior observed in the protein-protected Ag–Au alloy clusters.⁵⁹ For a better insight into PIA, the time evolution of TA is shown in Figure 6C. It reveals the long lifetime of carriers in the excited state, which does not decay in the time window of our instrument.¹⁹ Moreover, from the contour plot and spectral slices, it is also clear that the decay of excited states is accompanied by red-shifting of PIA with respect to the initial time scale, which indicates that PIA in different wavelength regimes consists of multiple components and arises from different states. Figure 6D–F shows the TA data of **1** in the water-aggregated state (f_w 70%). Unlike the monomeric form upon photoexcitation, the aggregated cluster showed a broad PIA. Although the TA features are the same, the spectrum consists of relatively fast decay profiles (Figure 6F) and a more pronounced red shift of PIA. Similar spectral features with contrasting temporal behavior of both samples suggest the presence of the same type of electronic transition in the monomeric and aggregated forms but with different

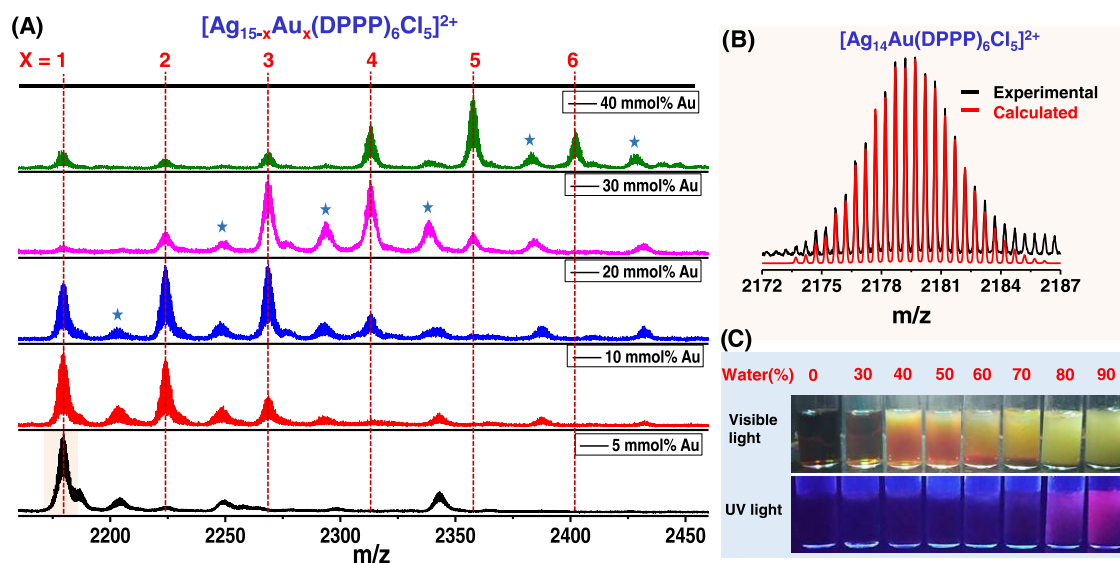


Figure 7. (A) Positive-mode ESI MS of $[\text{Ag}_{15-x}\text{Au}_x(\text{DPPP})_6\text{Cl}_5]^{2+}$, where $x = 1-6$, synthesized by varying the doped Au from 5 to 40 mmol %. The peaks labeled * refer to solvent (water and methanol) added peaks of the clusters. (B) Comparison of the experimental and calculated isotopic distributions of the cluster $[\text{Ag}_{15-x}\text{Au}_x(\text{DPPP})_6\text{Cl}_5]^{2+}$, when $x = 1$. (C) Photographs of the samples in different fractions of water under visible light and UV light, showing the solvent-induced aggregation property of the cluster.

rates of transitions. This is further supported by the same type of UV-vis spectra in their monomeric and water-aggregated states as shown in Figure S6. In addition, the TA data of cluster 1 in the solid state (thin film) are shown in Figure 6G–I. It also has similar TA features but a relatively very short lifetime of PIA in contrast to monomeric and water-aggregated forms. In fact, instead of the red shift of PIA, a blue shift takes place at a delayed time. Here, it is interesting to see that in all forms of cluster 1, the excited-state carriers mainly exhibit the PIA, and the lifetime of PIA decreases in water and even more in the solid state compared to its monomeric form.

Characterization of the $\text{Ag}_{15-x}\text{Au}_x$ Clusters. As we know, the size of the NCs is very much dependent on the ligand structure. Therefore, we have tried to synthesize the Ag–Au alloy NCs with different phosphines. We saw that among all of the phosphines studied (triphenylphosphine; bis(diphenylphosphino)methane; 1,2-bis(diphenylphosphino)ethane; 1,3-bis(diphenylphosphino)propane (DPPP); 1,4-bis(diphenylphosphino)butane (DPPB); 1,5-bis(diphenylphosphino)pentane, and 1,6-bis(diphenylphosphino)hexane), only DPPB and DPPP formed Ag–Au alloy clusters. Detailed synthetic procedure of $\text{Ag}_{15-x}\text{Au}_x$ protected with DPPP is given in the Experimental Section. During the synthesis of $\text{Ag}_{15-x}\text{Au}_x$, the concentration of incoming Au precursor was varied from 5 to 40 mmol %. Figure 7A represents the positive-mode HRESI MS data of $\text{Ag}_{15-x}\text{Au}_x$, where 5 mmol % Au doping shows the presence of a single major peak. For 10 mmol % Au doping, there were a group of peaks separated by m/z 44.5, and a total mass difference of $\Delta m = 44.5 \times 2 = 89$ ($z = 2$) appeared, corresponding to the mass difference between Au and Ag atoms. By increasing the doped Au concentration from 5 to 40 mmol %, a maximum of six Au atoms was possible to be incorporated, and the total composition was assigned as $[\text{Ag}_{15-x}\text{Au}_x(\text{DPPP})_6\text{Cl}_5]^{2+}$, where $x = 1-6$. The composition was also confirmed by the exact matching between the isotopic distributions of the experimental and calculated spectra as shown in Figure 7B. For this alloy cluster also, their methanol

solution was nonluminescent, and in the presence of water, it generated red luminescence. Corresponding photographs of the samples under visible and UV light are shown in Figure 7C, which show an increment in emission intensity from f_w 0 to 90%.

The UV-vis spectra of $\text{Ag}_{15-x}\text{Au}_x$ clusters are shown in Figure S10A. By increasing the fraction of Au, the peak positions were blue-shifted except for the peak at 495 nm. The blue shift was attributed to the increase in the HOMO–LUMO gap due to the modulation of their electronic structure during doping.^{16,19} During alloying with different mmol % of Au, $\text{Ag}_{11-x}\text{Au}_x$ showed a red shift, while $\text{Ag}_{15-x}\text{Au}_x$ showed a blue shift in the absorption spectra, which is attributed to the unique nature of the electronic perturbation upon incorporating Au at different positions. The alloy NCs $\text{Ag}_{15-x}\text{Au}_x$ were deep brown in color (inset of Figure S10A), and the solution was nonemissive to the naked eye and very weakly emissive in the PL spectrum (Figure S11). For ease of measurement, the alloy clusters with 5 mmol % gold doping labeled as 2 were selected for further characterization. Similar to 1, here also, we observed solid-state red luminescence after vacuum drying. Photographs of the solid-state cluster under visible and UV light are shown in Figure S10B. The PL spectrum showed an excitation peak at 395 nm and an emission peak at 660 nm, with a large Stokes shift. After 1 month, the PL intensity decreased from 6.16×10^6 to 5.07×10^6 (17%) (Figure S10C). UV-vis spectra of the same sample were also recorded before and after 1 month, which is shown in Figure S12.

In Figure S13, ^{31}P NMR data of 2 were compared with that of the ligand DPPP, and it confirmed the formation of a bond between phosphine and the alloy metal core. In Figure S14A, the XPS survey spectrum confirms the presence of C, O, P, Cl, Ag, and Au. The specific regions of Ag, Au, P, and Cl were deconvoluted in Figure S14B–E, respectively. For this alloy cluster also, the Ag $3d_{5/2}$ peak appeared slightly lower than that of Ag(0), and the Au $4f_{7/2}$ peak appeared higher than that of Au(0). TEM EDS analysis also confirmed the presence of Ag, Au, P, and Cl in 2 (Figure S15).

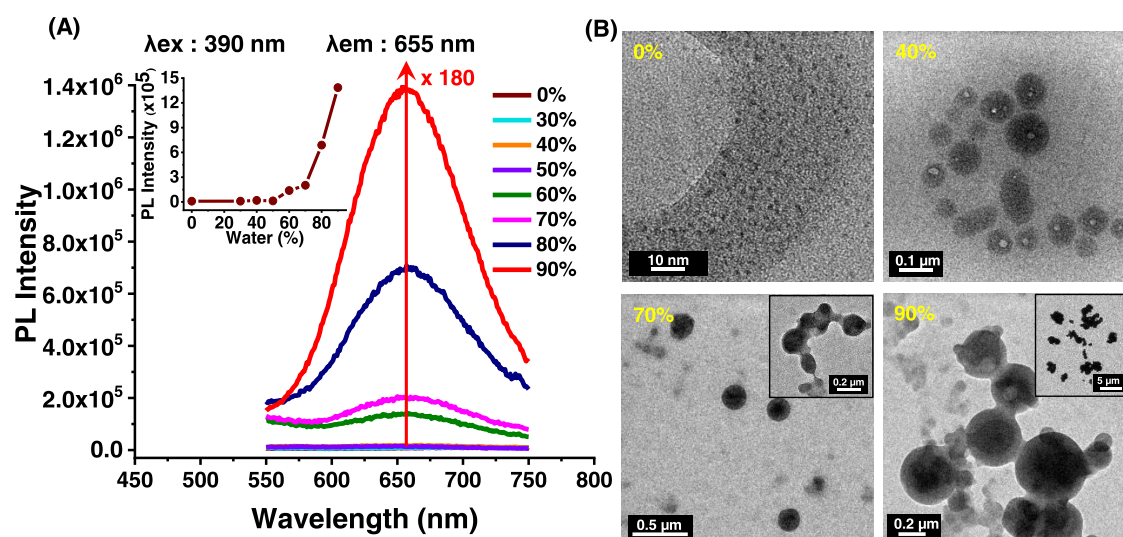


Figure 8. (A) PL emission spectra of **2** in methanol/water mixtures with different fractions of water. Inset: variation of luminescence intensity of the aggregates at different water fractions. (B) TEM images of **2** during the formation of solvent-induced aggregates in the presence of 0, 40, 70, and 90% water.

Solvent-Induced Aggregation of the $\text{Ag}_{15-x}\text{Au}_x$ Clusters. Similar to **1**, sample **2** too exhibited aggregation-induced emission in the solid state and in the presence of a methanol/water mixture. The emission peak was blue-shifted from 710 to 655 nm when f_w was varied from 0 to 90%. At f_w 60%, the emission peak centered at 655 nm started to appear, and it reached its maximum intensity at f_w 90% (Figure 8A) with 180-fold luminescence enhancement.⁶⁰ The inset of Figure 8A shows the variation of the PL intensity at 655 nm with changing fractions of water. For these samples, the peak positions in the UV–vis spectra (Figure S16) showed a small red shift during aggregate formation. With the initial increase of f_w values, there was a hyperchromic shift of the spectrum due to the formation of aggregates and background scattering. Further increment of f_w values causes much bigger particles to form with a hypochromic shift and broadening of the spectrum.²⁶ Here also, no change was observed in the absorption peak pattern. The aggregation process of both clusters **1** and **2** was reversible. Further, PL lifetime measurements were also carried out on cluster **2** and in the aggregated form. Results for the three different forms are plotted in Figure S17. Average lifetimes of 53.9 and 153.9 ns were obtained for the monomeric and water-aggregated states, respectively. For the solid state, the PL decay is dominated ($\approx 99\%$) by a fast decaying component, having a short lifetime compared to the IRF (≈ 400 ps). The rest consists of two slow-decaying components having lifetimes of ≈ 50 and 500 ns. The lifetimes observed are given in Table S2. The PL spectra of water-aggregated states of **2** were almost identical before and after oxygen exposure (Figure S18), which implies that this is a fluorescence phenomenon. The blue shift in PL emission from monomeric to the aggregated state also suggests that similar to **1**, here also, radiative decay at f_w 0% occurs from the low-lying singlet state to S_0 , and for f_w 70% and film, it occurs from the high-lying singlet state to S_0 . The PL decay pathway is similar to that in Figure 3C.

Characterization of the Aggregated Structures of $\text{Ag}_{15-x}\text{Au}_x$ Clusters. In Figure S19, the DLS data indicated that at f_w 30%, the average hydrodynamic diameter of the particle was ca. 60 nm, while for f_w 40–60%, they were 300–

400 nm, and for f_w 70–90%, the sizes became microscopic. TEM images were also investigated for different f_w , as shown in Figure 8B. For f_w 0%, there was the existence of only monomeric alloy NCs, and no aggregates were formed. The initial stage of formation of aggregates was noticed when f_w reached 40%, and the clusters were very loosely assembled in these 50–120 nm structures. At f_w 70%, the average size of the aggregated spheres was increased to 100–200 nm, and at some places, these spheres were connected (shown in the inset). For f_w 90%, the average sizes became 300 and 400 nm, and many of them were interconnected and precipitated by forming micrometer-sized aggregates (shown in the inset). This result is in accordance with the trend observed in the DLS data and PL spectra, where the larger and denser aggregates exhibited a higher luminescence intensity due to the large physical constraints of the ligands.

For an f_w value of 70%, the structures were closely studied with TEM and FESEM. Figure S20A represents some discrete spheres of aggregates under the transmission electron microscope. The high-magnification image in Figure S20B shows that these spheres are made by the assembly of small NCs, and they are hollow in nature. In contrast to **1**, here, the thickness of the peripheral domain was much higher compared to the interior domain, which can be due to the different ratios of hydrophilic and hydrophobic ligands present in these two NCs.⁵⁴ Figure S20C represents the TEM EDS of the aggregates. Figure S20D,E represents differently magnified FESEM images of a single sphere. The distribution of elements on a single sphere was examined by scanning the line profile in FESEM (Figure S20F), and all of the elements were successfully detected by it. The spatial distribution of these spheres was investigated by dark-field microscopy (Figure S20G) along with fluorescence microscopy (Figure S20H). As these particles have a tendency to connect with each other, the very bright spots observed in Figure S20G,H are likely to be due to the aggregation of multiple spheres. Figure S20I represents the measured average scattering spectrum centered at 510 nm.

TA Spectroscopy of the Monomeric and Aggregated Forms of $\text{Ag}_{15-x}\text{Au}_x$ Clusters. To understand the nature of

electronic transitions of **2**, TA spectroscopy has been performed, and Figure S21A–C shows a summary of the TA data at a pump fluence of 127 $\mu\text{J}/\text{cm}^2$ in methanol. The TA spectral profiles plotted for selected time delays in Figure S21B reveal that the excited state features are dominated by the PIA. However, here, a weak GSPB signal is present, corresponding to the phase-space filling of the absorption peak in the region of 500 nm in the UV–vis spectrum. Possibly, in contrast to **1**, GSPB in **2** arises due to a sharper and more prominent absorption peak at 500 nm. Further, the time evolution of PIA in Figure S21C reveals a fast decay profile and indicates a short lifetime of excited-state carriers in the **2**. Figure S21D–F presents the TA data of **2** after adding water (f_w 70%). It exhibits only PIA bands in the aggregated clusters, and no GSPB signal was observed. The time evolution of PIA in Figure S21F shows that the decay profile consists of an additional fast component at the early time compared to **2** in methanol and nearly the same time profile for the delayed time. The results of **2** in the solid state (thin film) are plotted in Figure S21G–I. It also shows nearly identical spectral and temporal features. From the obtained fs-TA results, it can be seen that compared to **1**, cluster **2** did not show much difference in the spectral and time evolution features in PIA among their monomeric, water-aggregated, and solid states. Possibly, the different behavior of clusters **1** and **2** is due to the different electronic structures corresponding to their different core compositions and ligands, which is also reflected in their different aggregation behavior at different water fractions.

Stability of the $\text{Ag}_{11-x}\text{Au}_x$ and $\text{Ag}_{15-x}\text{Au}_x$ Clusters. To check the stability of **1** and **2**, they were vacuum dried and stored at 4 °C. For the UV–vis characterization, the samples were dissolved in methanol, and the spectra were collected. The clusters exhibited the same absorption features, which reveals their higher stability, as shown in Figure S22.

CONCLUSIONS

In conclusion, we have reported the synthesis of two new series of phosphine- and chlorine-protected Ag–Au alloy NCs $[\text{Ag}_{11-x}\text{Au}_x(\text{DPPB})_5\text{Cl}_5\text{O}_2]^{2+}$, where $x = 1-10$, and $[\text{Ag}_{15-x}\text{Au}_x(\text{DPPP})_6\text{Cl}_5]^{2+}$, where $x = 1-6$. The use of two different phosphines resulted in the formation of two different cluster cores, which are more stable compared to the reported hydride- and phosphine-coprotected silver clusters. Interestingly, these nonluminescent phosphine-protected Ag–Au alloy clusters show solid-state and solvent-induced red luminescence due to AIE. For solvent-induced aggregation, different PL intensities were observed at varying solvent polarity, which is due to the formation of differently dense superstructures. Such spherical discrete hollow superstructures are formed by the assembly of alloy NCs, revealed by different microscopic studies performed on them. The more the density or compactness of the aggregated superstructures, the more the rigidification on the cluster surfaces results in enhanced emission. The mechanism of rigidification-induced emission was attributed to the modification in the excited-state relaxation pathways in the aggregated state of clusters. The degree of assembly of clusters to differently dense superstructures depends on the cluster core, ligand composition, and polarity of the solvents. Along with the extent of aggregation, the different behavior of these two alloy clusters is also reflected in their fs-TA spectroscopy results. As these cluster-assembled superstructures exhibit strong red luminescence with large Stokes shift and higher stability, they have great

potential in numerous applications like photonic materials, bioimaging or bio-labeling, sensors, etc. These hollow superstructures also can be used to encapsulate other functional molecules or nanoparticles. Thus, this work provides a new path for creating luminescent functional materials with atomically precise NCs as the building blocks.

EXPERIMENTAL SECTION

Chemicals. Silver nitrate (AgNO_3) was purchased from Rankem India. Tetrachloroauric acid trihydrate ($\text{HAuCl}_4 \cdot 3\text{H}_2\text{O}$) was prepared in our laboratory starting from elemental gold. 1,3-bis-(diphenylphosphino)propane (DPPP) and 1,4-bis-(diphenylphosphino)butane (DPPB) were purchased from Spectrochem. Sodium borohydride (NaBH_4 , 98%) was purchased from Sigma-Aldrich. All solvents, such as dichloromethane (DCM) and methanol (MeOH), were purchased from Rankem and were of high-performance liquid chromatography (HPLC) grade. Deuterated solvent CDCl_3 (99.8 atom % D) was purchased from Sigma-Aldrich for NMR measurements. All of the chemicals were used without further purification. Millipore water, obtained from Milli-Q (Millipore apparatus), was used for the experiments.

Synthesis of $[\text{Ag}_{11-x}\text{Au}_x(\text{DPPB})_5\text{Cl}_5\text{O}_2]^{2+}$, $x = 1-10$. Synthesis of DPPB-protected alloy metal clusters has been done, followed by the coreduction method, where mmol % of incoming metal precursor is varied. AgNO_3 and $\text{HAuCl}_4 \cdot 3\text{H}_2\text{O}$ of different mmol % were dissolved in 5 mL of MeOH by keeping the total metal ion concentration at 0.118 mmol (Table 1).

Table 1. Different mmol % of Ag and Au Precursors for $[\text{Ag}_{11-x}\text{Au}_x(\text{DPPB})_5\text{Cl}_5\text{O}_2]^{2+}$ ($x = 1-10$) Synthesis

mmol	5% Au	10% Au	20% Au	30% Au
AgNO_3	0.112	0.106	0.094	0.082
$\text{HAuCl}_4 \cdot 3\text{H}_2\text{O}$	0.006	0.0118	0.0236	0.0354

To the mixture of Ag and Au precursors, 75 mg of DPPB, dissolved in 9 mL of DCM, was added with constant stirring. After 20 min of stirring, 35 mg of NaBH_4 in 1 mL of ice-cold water was added. The addition of NaBH_4 immediately changed the color of the reaction mixture from almost colorless to brown. After 8 h of vigorous stirring under dark conditions, the color of the solution turned orange, and it was kept aside at 4 °C for 1 day. Then, the crude product was obtained by rotary evaporation, and the cluster was extracted with 10 mL of MeOH. During extraction, the solution was centrifuged two times at 8000 rpm for 5 min to remove excess DPPB as a precipitate. After that, the methanol solution was vacuum dried, and the cluster was cleaned one more time with DCM. Finally, the dried alloy cluster was dissolved in methanol and used for further characterization.

Synthesis of $[\text{Ag}_{15-x}\text{Au}_x(\text{DPPP})_6\text{Cl}_5]^{2+}$, $x = 1-6$. For the synthesis of the $[\text{Ag}_{15-x}\text{Au}_x(\text{DPPP})_6\text{Cl}_5]^{2+}$ cluster, the above-mentioned procedure was followed only by exchanging DPPB with DPPP and keeping all other chemicals the same. Here, mmol % of $\text{HAuCl}_4 \cdot 3\text{H}_2\text{O}$ was varied from 0 to 40% by keeping the total metal ion concentration at 0.118 mmol (Table 2).

After 8 h of continuous stirring in the dark, the reaction mixture became dark brown in color, and it was kept aside at 4 °C for 1 day. For cleaning this cluster, the above-mentioned procedure was followed. Finally, the dried alloy cluster was dissolved in methanol and used for further characterization.

Table 2. Different mmol % of Ag and Au Precursors for $[\text{Ag}_{15-x}\text{Au}_x(\text{DPPP})_6\text{Cl}_5]^{2+}$ ($x = 1-6$) Synthesis

mmol	5% Au	10% Au	20% Au	30% Au	40% Au
AgNO_3	0.112	0.106	0.094	0.082	0.071
$\text{HAuCl}_4 \cdot 3\text{H}_2\text{O}$	0.006	0.0118	0.0236	0.0354	0.0472

■ ASSOCIATED CONTENT

SI Supporting Information

The Supporting Information is available free of charge at <https://pubs.acs.org/doi/10.1021/acs.chemmater.2c03222>.

These data correspond to the instrumentation and characterization of the clusters and aggregates by UV–vis, ESI MS, NMR, XPS, DLS, HSI, FESEM, TEM, TCSPC, and fs-TA spectroscopy (PDF)

■ AUTHOR INFORMATION

Corresponding Authors

K. V. Adarsh – Department of Physics, Indian Institute of Science Education and Research Bhopal, Bhopal 462066, India; orcid.org/0000-0002-6337-6545; Email: adarsh@iiserb.ac.in

Thalappil Pradeep – DST Unit of Nanoscience (DST UNS) and Thematic Unit of Excellence (TUE), Department of Chemistry, Indian Institute of Technology Madras, Chennai 600036, India; International Centre for Clean Water, IIT Madras Research Park, Chennai 600113, India; orcid.org/0000-0003-3174-534X; Email: pradeep@iitm.ac.in

Authors

Madhuri Jash – DST Unit of Nanoscience (DST UNS) and Thematic Unit of Excellence (TUE), Department of Chemistry, Indian Institute of Technology Madras, Chennai 600036, India

Arijit Jana – DST Unit of Nanoscience (DST UNS) and Thematic Unit of Excellence (TUE), Department of Chemistry, Indian Institute of Technology Madras, Chennai 600036, India

Ajay K. Poonia – Department of Physics, Indian Institute of Science Education and Research Bhopal, Bhopal 462066, India; orcid.org/0000-0002-5551-7299

Esma Khatun – DST Unit of Nanoscience (DST UNS) and Thematic Unit of Excellence (TUE), Department of Chemistry, Indian Institute of Technology Madras, Chennai 600036, India

Papri Chakraborty – DST Unit of Nanoscience (DST UNS) and Thematic Unit of Excellence (TUE), Department of Chemistry, Indian Institute of Technology Madras, Chennai 600036, India; orcid.org/0000-0002-1353-7734

Ankit Nagar – DST Unit of Nanoscience (DST UNS) and Thematic Unit of Excellence (TUE), Department of Chemistry, Indian Institute of Technology Madras, Chennai 600036, India

Tripti Ahuja – DST Unit of Nanoscience (DST UNS) and Thematic Unit of Excellence (TUE), Department of Chemistry, Indian Institute of Technology Madras, Chennai 600036, India

Complete contact information is available at: <https://pubs.acs.org/doi/10.1021/acs.chemmater.2c03222>

Notes

The authors declare no competing financial interest.

■ ACKNOWLEDGMENTS

The authors thank the Department of Science and Technology, Government of India for constantly supporting our research program. M.J. thanks UGC for her senior research fellowship. A.J., E.K., A.N., and T.A. thank IIT Madras for their

research fellowships. P.C. thanks IIT Madras for an Institute Postdoctoral Fellowship. K.V.A. and A.K.P. gratefully acknowledge the Science and Engineering Research Board for the grant CRG/2019/002808.

■ REFERENCES

- (1) Wilcoxon, J. P.; Abrams, B. L. Synthesis, Structure and Properties of Metal Nanoclusters. *Chem. Soc. Rev.* **2006**, *35*, 1162–1194.
- (2) Jin, R.; Zeng, C.; Zhou, M.; Chen, Y. Atomically Precise Colloidal Metal Nanoclusters and Nanoparticles: Fundamentals and Opportunities. *Chem. Rev.* **2016**, *116*, 10346–10413.
- (3) Chakraborty, I.; Pradeep, T. Atomically Precise Clusters of Noble Metals: Emerging Link between Atoms and Nanoparticles. *Chem. Rev.* **2017**, *117*, 8208–8271.
- (4) Niihori, Y.; Eguro, M.; Kato, A.; Sharma, S.; Kumar, B.; Kurashige, W.; Nobusada, K.; Negishi, Y. Improvements in the Ligand-Exchange Reactivity of Phenylethanethiolate-Protected Au₂₅ Nanocluster by Ag or Cu Incorporation. *J. Phys. Chem. C* **2016**, *120*, 14301–14309.
- (5) Chen, S.; Higaki, T.; Ma, H.; Zhu, M.; Jin, R.; Wang, G. Inhomogeneous Quantized Single-Electron Charging and Electrochemical–Optical Insights on Transition-Sized Atomically Precise Gold Nanoclusters. *ACS Nano* **2020**, *14*, 16781–16790.
- (6) Li, Y.; Biswas, S.; Luo, T.-Y.; Juarez-Mosqueda, R.; Taylor, M. G.; Mpourmpakis, G.; Rosi, N. L.; Hendrich, M. P.; Jin, R. Doping Effect on the Magnetism of Thiolate-Capped 25-Atom Alloy Nanoclusters. *Chem. Mater.* **2020**, *32*, 9238–9244.
- (7) Song, Y.; Li, Y.; Zhou, M.; Liu, X.; Li, H.; Wang, H.; Shen, Y.; Zhu, M.; Jin, R. Ultrabright Au@Cu₁₄ Nanoclusters: 71.3% Phosphorescence Quantum Yield in Non-degassed Solution at Room Temperature. *Sci. Adv.* **2021**, *7*, No. eabd2091.
- (8) Zeng, C.; Li, T.; Das, A.; Rosi, N. L.; Jin, R. Chiral Structure of Thiolate-Protected 28-Gold-Atom Nanocluster Determined by X-ray Crystallography. *J. Am. Chem. Soc.* **2013**, *135*, 10011–10013.
- (9) Yuan, X.; Luo, Z.; Yu, Y.; Yao, Q.; Xie, J. Luminescent Noble Metal Nanoclusters as an Emerging Optical Probe for Sensor Development. *Chem.—Asian J.* **2013**, *8*, 858–871.
- (10) Liu, Y.; Yao, D.; Zhang, H. Self-Assembly Driven Aggregation-Induced Emission of Copper Nanoclusters: A Novel Technology for Lighting. *ACS Appl. Mater. Interfaces* **2018**, *10*, 12071–12080.
- (11) Xiao, Y.; Wu, Z.; Yao, Q.; Xie, J. Luminescent Metal Nanoclusters: Biosensing Strategies and Bioimaging Applications. *Aggregate* **2021**, *2*, 114–132.
- (12) Khatun, E.; Pradeep, T. New Routes for Multicomponent Atomically Precise Metal Nanoclusters. *ACS Omega* **2021**, *6*, 1–16.
- (13) Kang, X.; Zhu, M. Tailoring the Photoluminescence of Atomically Precise Nanoclusters. *Chem. Soc. Rev.* **2019**, *48*, 2422–2457.
- (14) van der Linden, M.; van Bunningen, A. J.; Amidani, L.; Bransen, M.; Elnaggar, H.; Glatzel, P.; Meijerink, A.; de Groot, F. M. F. Single Au Atom Doping of Silver Nanoclusters. *ACS Nano* **2018**, *12*, 12751–12760.
- (15) Ganguly, M.; Jana, J.; Pal, A.; Pal, T. Synergism of Gold and Silver Invites Enhanced Fluorescence for Practical Applications. *RSC Adv.* **2016**, *6*, 17683–17703.
- (16) Bootharaju, M. S.; Joshi, C. P.; Parida, M. R.; Mohammed, O. F.; Bakr, O. M. Templated Atom-Precise Galvanic Synthesis and Structure Elucidation of a [Ag₂₄Au(SR)₁₈][−] Nanocluster. *Angew. Chem., Int. Ed.* **2016**, *55*, 922–926.
- (17) Yu, Y.; Luo, Z.; Chevri er, D. M.; Leong, D. T.; Zhang, P.; Jiang, D.-E.; Xie, J. Identification of a Highly Luminescent Au₂₂(SG)₁₈ Nanocluster. *J. Am. Chem. Soc.* **2014**, *136*, 1246–1249.
- (18) Wang, S.; Meng, X.; Das, A.; Li, T.; Song, Y.; Cao, T.; Zhu, X.; Zhu, M.; Jin, R. A 200-fold Quantum Yield Boost in the Photoluminescence of Silver-Doped Ag_xAu_{25−x} Nanoclusters: The 13 th Silver Atom Matters. *Angew. Chem., Int. Ed.* **2014**, *53*, 2376–2380.

- (19) Soldan, G.; Aljuhani, M. A.; Bootharaju, M. S.; Abdul-Halim, L. G.; Parida, M. R.; Emwas, A.-H.; Mohammed, O. F.; Bakr, O. M. Gold Doping of Silver Nanoclusters: A 26-Fold Enhancement in the Luminescence Quantum Yield. *Angew. Chem., Int. Ed.* **2016**, *55*, 5749–5753.
- (20) Niesen, B.; Rand, B. P. Thin Film Metal Nanocluster Light-Emitting Devices. *Adv. Mater.* **2014**, *26*, 1446–1449.
- (21) Koh, T. W.; Hiszpanski, A. M.; Sezen, M.; Naim, A.; Galfsky, T.; Trivedi, A.; Loo, Y. L.; Menon, V.; Rand, B. P. Metal Nanocluster Light-emitting Devices with Suppressed Parasitic Emission and Improved Efficiency: Exploring the Impact of Photophysical Properties. *Nanoscale* **2015**, *7*, 9140–9146.
- (22) Wang, Z.; Chen, B.; Zhu, M.; Kershaw, S. V.; Zhi, C.; Zhong, H.; Rogach, A. L. Stretchable and Thermally Stable Dual Emission Composite Films of On-Purpose Aggregated Copper Nanoclusters in Carboxylated Polyurethane for Remote White Light-Emitting Devices. *ACS Appl. Mater. Interfaces* **2016**, *8*, 33993–33998.
- (23) Huang, R.-W.; Wei, Y.-S.; Dong, X.-Y.; Wu, X.-H.; Du, C.-X.; Zang, S.-Q.; Mak, T. C. W. Hypersensitive Dual-function Luminescence Switching of a Silver-chalcogenolate Cluster-based Metal–organic Framework. *Nat. Chem.* **2017**, *9*, 689–697.
- (24) Wang, Y.-M.; Zhang, J.-W.; Wang, Q.-Y.; Li, H.-Y.; Dong, X.-Y.; Wang, S.; Zang, S.-Q. Fabrication of Silver Chalcogenolate Cluster Hybrid Membranes with Enhanced Structural Stability and Luminescence Efficiency. *Chem. Commun.* **2019**, *55*, 14677–14680.
- (25) Zhao, M.; Qian, Z.; Zhong, M.; Chen, Z.; Ao, H.; Feng, H. Fabrication of Stable and Luminescent Copper Nanocluster-Based AIE Particles and Their Application in β -Galactosidase Activity Assay. *ACS Appl. Mater. Interfaces* **2017**, *9*, 32887–32895.
- (26) Luo, Z.; Yuan, X.; Yu, Y.; Zhang, Q.; Leong, D. T.; Lee, J. Y.; Xie, J. From Aggregation-Induced Emission of Au(I)–Thiolate Complexes to Ultrabright Au(0)@Au(I)–Thiolate Core–Shell Nanoclusters. *J. Am. Chem. Soc.* **2012**, *134*, 16662–16670.
- (27) Goswami, N.; Yao, Q.; Luo, Z.; Li, J.; Chen, T.; Xie, J. Luminescent Metal Nanoclusters with Aggregation-Induced Emission. *J. Phys. Chem. Lett.* **2016**, *7*, 962–975.
- (28) Chang, H.; Karan, N. S.; Shin, K.; Bootharaju, M. S.; Nah, S.; Chae, S. I.; Baek, W.; Lee, S.; Kim, J.; Son, Y. J.; Kang, T.; Ko, G.; Kwon, S.-H.; Hyeon, T. Highly Fluorescent Gold Cluster Assembly. *J. Am. Chem. Soc.* **2021**, *143*, 326–334.
- (29) Li, Q.; Zhou, M.; So, W. Y.; Huang, J.; Li, M.; Kauffman, D. R.; Cotlet, M.; Higaki, T.; Peteanu, L. A.; Shao, Z.; Jin, R. A Monocuboctahedral Series of Gold Nanoclusters: Photoluminescence Origin, Large Enhancement, Wide Tunability, and Structure–Property Correlation. *J. Am. Chem. Soc.* **2019**, *141*, 5314–5325.
- (30) Wang, Z.; Xiong, Y.; Kershaw, S. V.; Chen, B.; Yang, X.; Goswami, N.; Lai, W.-F.; Xie, J.; Rogach, A. L. In Situ Fabrication of Flexible, Thermally Stable, Large-Area, Strongly Luminescent Copper Nanocluster/Polymer Composite Films. *Chem. Mater.* **2017**, *29*, 10206–10211.
- (31) Xie, Z.; Sun, P.; Wang, Z.; Li, H.; Yu, L.; Sun, D.; Chen, M.; Bi, Y.; Xin, X.; Hao, J. Metal–Organic Gels from Silver Nanoclusters with Aggregation-Induced Emission and Fluorescence-to-Phosphorescence Switching. *Angew. Chem., Int. Ed.* **2020**, *59*, 9922–9927.
- (32) Luo, J.; Xie, Z.; Lam, J. W. Y.; Cheng, L.; Chen, H.; Qiu, C.; Kwok, H. S.; Zhan, X.; Liu, Y.; Zhu, D.; Tang, B. Z. Aggregation-induced Emission of 1-methyl-1,2,3,4,5-pentaphenylsilole. *Chem. Commun.* **2001**, 1740–1741.
- (33) Kolay, S.; Bain, D.; Maity, S.; Devi, A.; Patra, A.; Antoine, R. Self-Assembled Metal Nanoclusters: Driving Forces and Structural Correlation with Optical Properties. *Nanomaterials* **2022**, *12*, No. 544.
- (34) Rival, J. V.; Mymoon, P.; Lakshmi, K. M.; Nonappa; Pradeep, T.; Shibu, E. S. Self-Assembly of Precision Noble Metal Nanoclusters: Hierarchical Structural Complexity, Colloidal Superstructures, and Applications. *Small* **2021**, *17*, No. 2005718.
- (35) Bera, D.; Goswami, N. Driving Forces and Routes for Aggregation-Induced Emission-Based Highly Luminescent Metal Nanocluster Assembly. *J. Phys. Chem. Lett.* **2021**, *12*, 9033–9046.
- (36) Wu, Z.; Yao, Q.; Zang, S.; Xie, J. Directed Self-Assembly of Ultrasmall Metal Nanoclusters. *ACS Mater. Lett.* **2019**, *1*, 237–248.
- (37) Krishnadas, K. R.; Natarajan, G.; Bakshi, A.; Ghosh, A.; Khatun, E.; Pradeep, T. Metal–Ligand Interface in the Chemical Reactions of Ligand-Protected Noble Metal Clusters. *Langmuir* **2019**, *35*, 11243–11254.
- (38) Wu, Z.; Du, Y.; Liu, J.; Yao, Q.; Chen, T.; Cao, Y.; Zhang, H.; Xie, J. Auophilic Interactions in the Self-Assembly of Gold Nanoclusters into Nanoribbons with Enhanced Luminescence. *Angew. Chem., Int. Ed.* **2019**, *58*, 8139–8144.
- (39) Chakraborty, S.; Bain, D.; Maity, S.; Kolay, S.; Patra, A. Controlling Aggregation-Induced Emission in Bimetallic Gold–Copper Nanoclusters via Surface Motif Engineering. *J. Phys. Chem. C* **2022**, *126*, 2896–2904.
- (40) Wu, Z.; Liu, J.; Gao, Y.; Liu, H.; Li, T.; Zou, H.; Wang, Z.; Zhang, K.; Wang, Y.; Zhang, H.; Yang, B. Assembly-Induced Enhancement of Cu Nanoclusters Luminescence with Mechanochromic Property. *J. Am. Chem. Soc.* **2015**, *137*, 12906–12913.
- (41) Sugiuchi, M.; Maeba, J.; Okubo, N.; Iwamura, M.; Nozaki, K.; Konishi, K. Aggregation-Induced Fluorescence-to-Phosphorescence Switching of Molecular Gold Clusters. *J. Am. Chem. Soc.* **2017**, *139*, 17731–17734.
- (42) Sugiuchi, M.; Zhang, M.; Hakoishi, Y.; Shichibu, Y.; Horimoto, N. N.; Yamauchi, Y.; Ishida, Y.; Konishi, K. Aggregation-Mode-Dependent Optical Properties of Cationic Gold Clusters: Formation of Ordered Assemblies in Solution and Unique Optical Responses. *J. Phys. Chem. C* **2020**, *124*, 16209–16215.
- (43) Bootharaju, M. S.; Kozlov, S. M.; Cao, Z.; Harb, M.; Maity, N.; Shkurenko, A.; Parida, M. R.; Hedhili, M. N.; Eddooudi, M.; Mohammed, O. F.; Bakr, O. M.; Cavallo, L.; Basset, J.-M. Doping-Induced Anisotropic Self-Assembly of Silver Icosahedra in $[\text{Pt}_2\text{Ag}_{23}\text{Cl}_7(\text{PPh}_3)_{10}]$ Nanoclusters. *J. Am. Chem. Soc.* **2017**, *139*, 1053–1056.
- (44) Jash, M.; Khatun, E.; Chakraborty, P.; Sudhakar, C.; Pradeep, T. $[\text{Ag}_{15}\text{H}_{13}(\text{DPPH})_5]^{2+}$ and $[\text{Ag}_{27}\text{H}_{22}(\text{DPPB})_7]^{3+}$: Two New Hydride and Phosphine Co-Protected Clusters and Their Fragmentation Leading to Naked Clusters, Ag_{13}^+ and Ag_{25}^+ . *J. Phys. Chem. C* **2020**, *124*, 20569–20577.
- (45) Mishra, D.; Lobodin, V.; Zhang, C.; Aldeek, F.; Lochner, E.; Mattoussi, H. Gold-doped Silver Nanoclusters with Enhanced Photophysical Properties. *Phys. Chem. Chem. Phys.* **2018**, *20*, 12992–13007.
- (46) Negishi, Y.; Iwai, T.; Ide, M. Continuous Modulation of Electronic Structure of Stable Thiolate-protected Au_{25} Cluster by Ag Doping. *Chem. Commun.* **2010**, *46*, 4713–4715.
- (47) Negishi, Y.; Nobusada, K.; Tsukuda, T. Glutathione-Protected Gold Clusters Revisited: Bridging the Gap between Gold(I)–Thiolate Complexes and Thiolate-Protected Gold Nanocrystals. *J. Am. Chem. Soc.* **2005**, *127*, 5261–5270.
- (48) Ihm, H.; Ahn, J.-S.; Lah, M. S.; Ko, Y. H.; Paek, K. Oligobisvelcralex: Self-Assembled Linear Oligomer by Solvophobic π – π Stacking Interaction of Bisvelcralex Based on Resorcin[4]arene. *Org. Lett.* **2004**, *6*, 3893–3896.
- (49) Kang, X.; Wang, S.; Zhu, M. Observation of a New Type of Aggregation-induced Emission in Nanoclusters. *Chem. Sci.* **2018**, *9*, 3062–3068.
- (50) Sun, P.-P.; Han, B.-L.; Li, H.-G.; Zhang, C.-K.; Xin, X.; Dou, J.-M.; Gao, Z.-Y.; Sun, D. Real-Time Fluorescent Monitoring of Kinetically Controlled Supramolecular Self-Assembly of Atom-Precise Cu_8 Nanocluster. *Angew. Chem., Int. Ed.* **2022**, *61*, No. e202200180.
- (51) Das, P.; Kumar, A.; Chowdhury, A.; Mukherjee, P. S. Aggregation-Induced Emission and White Luminescence from a Combination of π -Conjugated Donor–Acceptor Organic Luminescences. *ACS Omega* **2018**, *3*, 13757–13771.
- (52) Zhu, C.; Xin, J.; Li, J.; Li, H.; Kang, X.; Pei, Y.; Zhu, M. Fluorescence or Phosphorescence? The Metallic Composition of the Nanocluster Kernel Does Matter. *Angew. Chem., Int. Ed.* **2022**, *61*, No. e202205947.

(53) Deng, H.-H.; Shi, X.-Q.; Wang, F.-F.; Peng, H.-P.; Liu, A.-L.; Xia, X.-H.; Chen, W. Fabrication of Water-Soluble, Green-Emitting Gold Nanoclusters with a 65% Photoluminescence Quantum Yield via Host–Guest Recognition. *Chem. Mater.* **2017**, *29*, 1362–1369.

(54) Park, J.-e.; Seo, M.; Jang, E.; Kim, H.; Kim, J. S.; Park, S.-J. Vesicle-like Assemblies of Ligand-stabilized Nanoparticles with Controllable Membrane Composition and Properties. *Nanoscale* **2019**, *11*, 1837–1846.

(55) Nonappa; Lahtinen, T.; Haataja, J. S.; Tero, T.-R.; Häkkinen, H.; Ikkala, O. Template-Free Supracolloidal Self-Assembly of Atomically Precise Gold Nanoclusters: From 2D Colloidal Crystals to Spherical Capsids. *Angew. Chem., Int. Ed.* **2016**, *55*, 16035–16038.

(56) Hou, Y.; Wang, Y.; Xu, T.; Wang, Z.; Tian, W.; Sun, D.; Yu, X.; Xing, P.; Shen, J.; Xin, X.; Hao, J. Synergistic Multiple Bonds Induced Dynamic Self-Assembly of Silver Nanoclusters into Lamellar Frameworks with Tailored Luminescence. *Chem. Mater.* **2022**, *34*, 8013–8021.

(57) Jülicher, F.; Lipowsky, R. Domain-induced Budding of Vesicles. *Phys. Rev. Lett.* **1993**, *70*, 2964–2967.

(58) Zhou, Y.; Zeng, H. C. Simultaneous Synthesis and Assembly of Noble Metal Nanoclusters with Variable Micellar Templates. *J. Am. Chem. Soc.* **2014**, *136*, 13805–13817.

(59) Bhunia, S.; Kumar, S.; Purkayastha, P. Dependence of Ultrafast Dynamics in Gold–silver Alloy Nanoclusters on the Proportion of the Metal Content. *SN Appl. Sci.* **2019**, *1*, No. 449.

(60) Jin, S.; Liu, W.; Hu, D.; Zou, X.; Kang, X.; Du, W.; Chen, S.; Wei, S.; Wang, S.; Zhu, M. Aggregation-Induced Emission (AIE) in Ag–Au Bimetallic Nanocluster. *Chem.—Eur. J.* **2018**, *24*, 3712–3715.